An inversion approach for analysing the physical properties of a seismic low-velocity layer in the upper mantle

Jie Xiao, Saswata Hier-Majumder, Benoit Tauzin, Dave Waltham

An inversion approach for analysing the physical properties of a seismic low-velocity layer in the upper mantle

Jie Xiao[a, b, c,*], Saswata Hier-Majumder[b], Benoit Tauzin[d, e], Dave Waltham[b]

(a) State Key Laboratory of Organic Geochemistry, Guangzhou Institute of Geochemistry, Chinese Academy of Sciences, Guangzhou, 510640, China

(b) Department of Earth Sciences, Royal Holloway, University of London, Egham, TW20 0EX, United Kingdom

(c) University of Chinese Academy of Sciences, Beijing 100049, China

(d) Université de Lyon, UCBL, ENS Lyon, CNRS, Laboratoire de Géologie de Lyon, Terre, Planètes, Environnement, Villeurbanne, France

(e) Research School of Earth Sciences, Australian National University, Canberra, Australian Capital Territory 0200, Australia

* Corresponding author (Jie.Xiao.2016@live.rhul.ac.uk)

Abstract

In this article, we propose a new inversion scheme to calculate the melt volume fractions from observed seismic anomalies in a low-velocity layer (LVL) located atop the mantle transition zone. Our method identifies the trade-offs in the seismic signature caused by temperature, solid composition, melt volume fraction, and dihedral angle at the solid-melt interface. Using the information derived from the amplitude of *P*-to-*S* conversions beneath the western US, we show that the multiple

permissible solutions for melt volume fractions are correlated to each other. An existing solution can be directly transformed into a different solution whilst leaving the model output unaltered. Hence, the additional solutions can be rapidly derived given an initial solution. The calculation of multiple solutions reveals the universal properties to the whole range of solutions. A regional-averaged melt volume fraction of at least 0.5% exists in every solution. In addition, the mantle potential temperature in the western US is broadly lower than 1550 K and the LVL in this region tends to be basaltic-rich. Using these insights, it is possible to give firm statements on the LVL and the solid mantle even though a unique interpretation does not exist.

Keywords: Shear wave, low-velocity layer, partial melting, inverse problem, non-uniqueness

1 Introduction

The mantle transition zone (MTZ), marked by a drastic change in the physical properties of the silicate mineral phases, plays a crucial role in the convective flow within the mantle. Owing to the sharp changes in density and volatile storage capacity across the boundaries of the MTZ, it can act as an impediment to mass transfer and sights of partial melting (Bercovici and Karato, 2003; Morra et al., 2010). Indirect evidence of mass transfer between subducting slabs and surrounding mantle are obtained from the so-called 'superdeep diamonds' which bear geochemical signature of oxygen and carbon isotopic ratios that can be generated by mixing between mantle

45 and subducting slabs at these depths. Seismic observations also support the evidence
46 of partial melting atop the MTZ. A low-velocity layer (LVL) located at ~350 km depth
47 has been identified just above the mantle transition zone in numerous regions around
48 the world, with lateral thickness from tens to over a few hundred kilometres (e.g. Song
49 et al., 2004; Gao et al., 2006; Courtier and Revenaugh, 2007; Schaeffer and Bostock,
50 2010; Huckfeldt et al., 2013). Characterized by 2 – 3% reductions in shear wave
51 velocities, the LVL is characterized by a sharp interface with the overlying mantle,
52 indicating the likely presence of a chemical anomaly, in particular partial melting.
53 However, quantifying the fraction of melt has remained challenging as the
54 environmental and chemical parameters, such as the mantle temperature, bulk solid
55 composition and melt geometry, are not clearly understood.

56 The 350-km LVL has been frequently interpreted as a seismic signature of a small
57 fraction of melt triggered by volatile elements released from subduction zones
58 (Revenaugh and Sipkin, 1994) or mantle plumes (Vinnik and Farra, 2007). Since melts,
59 characterized by zero shear modulus, disproportionately reduce shear wave velocities,
60 seismic anomalies with low velocities are often qualitatively attributed to melting.
61 Interpreting the origin of the seismic velocity anomalies in the LVL is complicated due
62 to the competing influence of several parameters. While an increase in the
63 temperature typically leads to seismic velocity reductions, the influence of bulk mantle
64 composition on seismic velocities varies with depth (Xu et al., 2008). The multiple
65 factors also likely affect each other. For instance, melting may leave a strong impact on
66 the bulk solid composition, in particular the amount of basalt. The residual anomaly,

67 defined as the difference between the observed shear velocity and the reference
68 velocity, can be attributed to the presence of melting, and used as a basis for
69 calculating the volume fraction of melt in the LVL. Hence, calculation of the melt
70 fraction requires accurate estimation of the reference seismic velocities, i.e. velocities
71 in the absence of melting for given temperature and solid composition.
72 In addition, the non-uniqueness in the LVL interpretations arises from the fact
73 that, in a partially molten layer, the seismic velocity reductions depend on both the
74 melting extent and the microstructure of the melt-bearing aggregates (Mavko, 1980;
75 von Bargen and Waff, 1986; Takei, 1998, 2002). The dihedral angle (also known as
76 wetting angle) at the solid-melt interface, controls the geometry of the load-bearing
77 framework of partially molten rocks (Hier-Majumder and Abbott, 2010), trading off
78 with inferred melt volume fraction . The chemical composition is also found to play a
79 moderate role in reducing the seismic speeds (Wimert and Hier-Majumder, 2012; Hier-
80 Majumder et al., 2014), and may alter the dihedral angle (Yoshino et al., 2005). The
81 numerical experiment of (Hier-Majumder et al., 2014) indicated the difficulties in
82 distinguishing different types of melt from the seismic observations as the fraction of
83 melt is very small. These therefore lead to extra non-uniqueness in the interpretation
84 of seismic anomalies.
85 A number of previous studies mitigated the issue of competing influences by
86 carrying out computationally expensive brute-force search to create lookup tables for
87 inferred melt volume fractions corresponding to different controlling factors (e.g. Hier-
88 Majumder and Courtier, 2011; Hier-Majumder et al., 2014; Hier-Majumder and Tauzin,

89 2017). While a brute-force search can produce a particular scenario of inversion,
90 application of the approach is unable to ascertain if alternative solutions exist in the
91 parameter space. Although, in principle, the entire range of solutions could be
92 discovered through repetitive use of the algorithm given different combinations of the
93 parameters, it fails to rigorously tackle the nature of variations in the inferred melt
94 volume fractions caused by changes in the other factors. Therefore, a new inversion
95 scheme is required to interpret these geophysical observations and to address the
96 theoretical drawback of previous studies.

97 Here we present a mathematical formulation that uses the implicit symmetry of a
98 petrologic model to understand the non-uniqueness in the melt fraction inference. The
99 results from our work provide a more reliable evaluation of the long-standing problem
100 in rock physics. The principle of symmetry has been successfully applied in a sequence
101 stratigraphic problem (Xiao and Waltham, 2019), showing that the whole set of
102 solutions are closely linked even when an inverse problem is non-linear. An existing
103 solution can be directly transformed into another solution that leaves modelling
104 products unchanged, in the same way that rotating a square by 90° can produce an
105 identical geometry. In this way, the search for all possible solutions can begin with an
106 initial solution generated through standard inversion techniques. The application of
107 the symmetry method can then allow the additional solutions to be calculated from
108 the initial solution.

109 Embedded with a predictive forward model of shear-velocities, our inversion
110 scheme is used to revisit the nature of the 350-km LVL beneath the western US. The

seismically anomalous layer in this region has been reported underneath the Oregon-Washington border (e.g. Song et al., 2004), the Yellowstone (e.g. Fee and Dueker, 2004; Jasbinsek and Dueker, 2007), the Northern Rocky Mountains (e.g. Jasbinsek and Dueker, 2007; Zhang et al., 2018), the Colorado Plateau/Rio Grande Rift (e.g. Jasbinsek et al., 2010), and California (e.g. Vinnik et al., 2010). Once the complete set of solutions has been derived, the lowest and highest possible fractions of melt within the LVL can be easily determined. As such, we can generate a robust statement on the partial melting effect in the LVL that does not rely on assumed values of the other parameters. The calculation can also offer more reliable information about the solid mantle, such as the plausible ranges of temperature and basalt fraction. For example, the estimates of melt content and associated parameters can be used to infer the budget of volatile elements in the mantle and the excess temperature of the mantle plumes beneath the region.

2 The 350-km LVL beneath the western US

2.1 Seismic observations

The seismic data used here are teleseismic *P*-to-*S* conversions recorded on receiver functions from the Transportable Array of seismic stations in the western US (fig. 1). The portion of the seismic network consists in 820 seismic stations. Shear wave velocity contrasts at around 350 km have been derived for 583 sites over a 0.5° x 0.5° grid in latitude and longitude. The seismically anomalous layer covers an area of 1.8 × 10^6 km^2, with lateral thickness from 25 to 90 km (Hier-Majumder and Tauzin, 2017).

2.2 Calculating shear wave velocities

To invert the shear wave speeds in the LVL from the seismic observations, we follow the computational approach outlined in Hier-Majumder et al. (2014). We use the results of conversion amplitudes at the top and the base of the LVL to estimate the velocity variations. To eliminate systematic variations in the amplitude of converted arrivals caused by the acquisition geometry (seismic wave incidence), we normalize the observed seismic amplitudes prior to computation. The normalized amplitude is calculated from the ratio of amplitudes of arrivals converted at the top of the LVL over arrivals converted at the olivine-wadsleyite mineralogical phase change at 410 km depth:

$$R_{\mathrm{norm}} = \frac{A_{\mathrm{LVL}}}{A_{410}} < 0 \tag{1}$$

, where A_{LVL} is the frequency-averaged amplitude at the top of the LVL recorded at each cell on the grid, and A_{410} is the frequency-averaged amplitude at the 410-km discontinuity in the same cell. Using the normalized R_{norm}, we then calculate the shear wave velocity ($V_{\mathrm{S}}^{\mathrm{obs}}$) at each location from the normalized contrast between the shear-velocity immediately above the 350-km LVL (V_{S}^{350}) and the velocity immediately below the 410-km discontinuity (V_{S}^{410}):

$$V_{\mathrm{S}}^{\mathrm{obs}} = V_{\mathrm{S}}^{350}\left(1 + R_{\mathrm{norm}}\frac{V_{\mathrm{S}}^{410} - V_{\mathrm{S}}^{350}}{V_{\mathrm{S}}^{350}}\right) \tag{2}$$

We calculate V_{S}^{350} and V_{S}^{410} as the shear wave velocities at the depths of 350 km and 410 km, respectively, from the Preliminary Reference Earth Model (PREM, Dziewonski

and Anderson, 1981). Compared to the global predictions from the PREM (~4735m/s at 350 km depth), the estimated shear-velocities yield an average reduction of 1.6%.

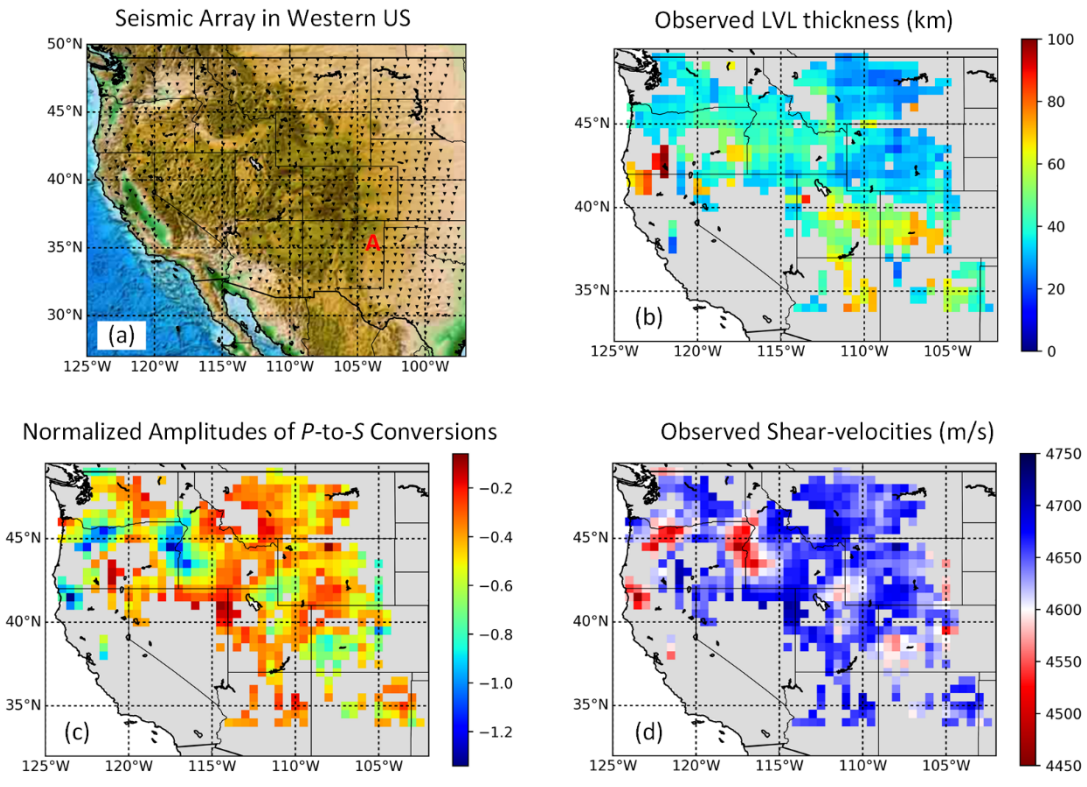

Figure 1 Seismic observations of the 350-km LVL below the western US. (a) A map of the dense seismic array of 820 sites (black triangles, from Tauzin et al., 2013). The seismic cell (106.5°W, 38°N) discussed later in this paper is labelled 'A'. (b) The 350-km LVL with lateral thickness is identified beneath 583 sites (from Hier-Majumder and Tauzin, 2017). (c) Normalized amplitudes of *P*-to-*S* converted arrivals. (d) Shear wave velocities in the LVL estimated from the seismic data

2.3 Evaluating relative temperature variations

We then evaluate the thermal variations in the LVL using the method outlined in Tauzin and Ricard (2014). In this method, the relative temperature variations (ΔT) on boundary topography are correlated with the relative thickness of the MTZ (δh) and

the Clapeyron slopes (i.e. the change in temperature of phase transition with respect to the change in pressure at which the phase transition occurs) for the olivine-wadsleyite phase transitions at 410 km (γ_{410}) and 660 km (γ_{660}). We employ the data of spatial variations in MTZ thickness beneath the western half of the US from Tauzin et al. (2013). We also set the reference MTZ thickness at 250 km as Tauzin and Ricard (2014) calculated from the IASP91 spherical model of Kennett and Engdahl (1991). We follow the empirical scheme of Tauzin and Ricard (2014) and set γ_{410} = 3.0 MPa/K and γ_{660} = 0.64 γ_{410} – 1.17. The uncertainties associated with the supplementary parameters will be discussed in later sections. Using these methods, we calculate the temperature variations in the LVL from the MTZ thickness beneath the seismic array.

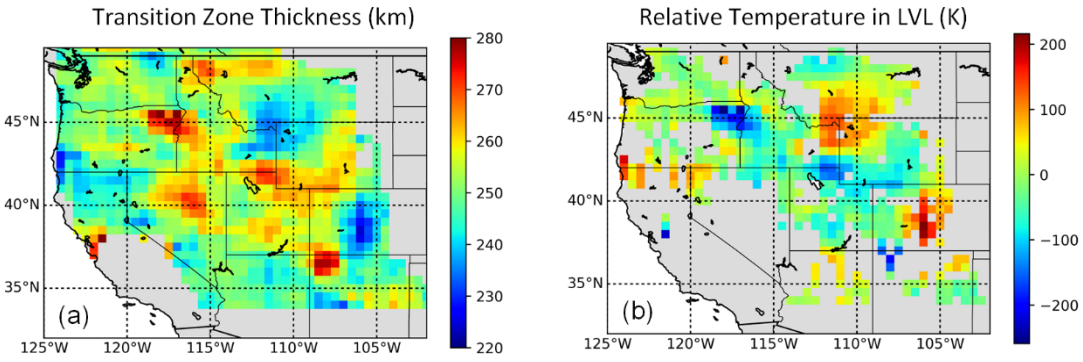

Figure 2 Thickness of MTZ (a) and relative temperature variations in the LVL (b) estimated from the MTZ thickness (after Tauzin and Ricard, 2014)

3 Forward modelling

The forward model of shear-velocities presented here incorporates four primary controls, including the mantle potential temperature, bulk solid composition, melt volume fraction and dihedral angle at the solid-melt interface. The simulation of shear

wave speeds in the LVL consists of two independent phases. Firstly, we estimate the reference velocities from the properties of the solid mantle. Secondly, we calculate the changes in velocities as waves travelling through a melt-bearing aggregate using a micromechanical model that involves both the fraction and geometry of the melt.

3.1 Estimating reference velocities

We estimate the reference shear wave speeds in the solid mantle accounting for the thermal and compositional properties of the mineral. The mantle temperature below each site can be expressed as

$$T = T_0 + \frac{\mathrm{dT}}{\mathrm{dz}} z_{\mathrm{LVL}} + \Delta T \tag{3}$$

, where T_0 is the potential temperature of the reference mantle, $\mathrm{d}T/\mathrm{d}z$ is the adiabatic temperature gradient which is suggested as 0.4 – 0.5 K/km in the upper mantle (Katsura et al., 2010), z_{LVL} is the depth of LVL and ΔT is the relative temperature variation at a given location. We set z_{LVL} at the average depth of 352 km as observed from the seismic profiles. To quantify the mantle composition, we follow the definition from Xu et al. (2008) which parameterizes the solid bulk as a mechanical mixture of mid-ocean ridge basalt and harzburgite. The composition of the solid mantle can therefore be expressed as the volume fraction of basaltic component. We can then formulate the reference shear wave velocities as $V_{\mathrm{S}}^{\mathrm{ref}} = V_{\mathrm{S}}^{\mathrm{ref}}(T_0, C)$, where T_0 and C are the potential temperature and basalt fraction of the mantle, respectively.

Reference shear wave speeds applied here are derived from the mineral physics database of Xu et al. (2008), in which seismic velocities are tabulated with associated combinations of potential temperatures and basalt fractions. In the database, potential temperatures range from 1000 to 2000 K with increments of 100 K whereas basalt fractions range from 0 to 100% with increments of 5%. While we can select a given value of C for the calculation, the temperature at any point on the seismic grid is determined from the MTZ thickness as discussed above. As a result, we interpolate the value of seismic velocity for the temperature evaluated at each location using a second-order polynomial interpolation between two tabulated values. Using this interpolation, we are able to calculate the value of reference shear wave speed at each point for a given bulk basalt volume fraction and a given reference potential temperature. Figure 3 presents the predictions of regional-average shear wave speeds for a range of potential temperatures and basalt fractions at a constant pressure of 11.7 GPa. The thermal and compositional effects can trade off with each other and thus different combinations of the two variables may lead to the same velocities.

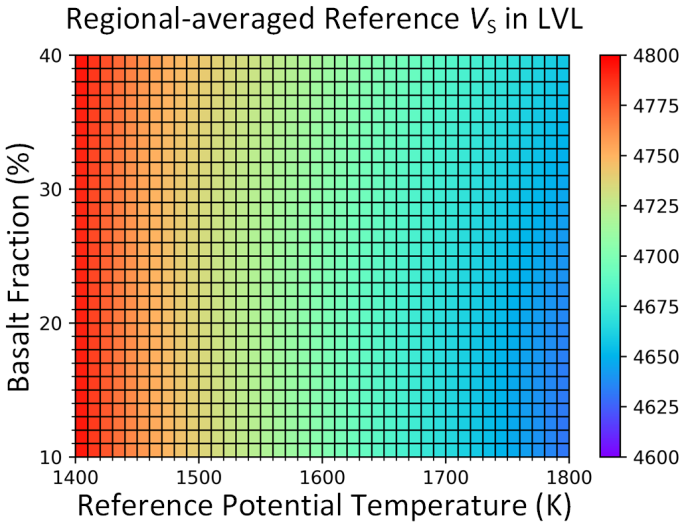

Figure 3 A heatmap showing the predicted regional-averaged reference shear wave velocities at 11.7 GPa in response to different combinations of reference potential temperature and basalt fraction in the LVL beneath the western US

3.2 Partial melting and velocity reductions

To simulate the influence of partial melting on seismic velocities, we employ the modelling scheme of Takei (2002), where the shear wave speed variation ξ is governed by the effective elastic moduli of the aggregate:

$$\xi = \sqrt{\frac{N/\mu}{\bar{\rho}/\rho_s}} \tag{4}$$

, where N is the elastic modulus of the intergranular skeletal framework that indicates the strength of contact between the neighbouring grains; μ is the shear modulus; ρ_s is the density of the solid bulk; and $\bar{\rho}$ is the volume-averaged density of the entire aggregate which is calculated as:

$$\bar{\rho} = \rho_m \varphi + \rho_s (1 - \varphi) \tag{5}$$

, where ρ_m is the density of the melt; φ is the volume fraction of melt within the aggregate.

In eq. 4, the elastic modulus N is determined by both the melt volume fraction φ and the contiguity (ψ, i.e. the area fraction of the intergranular contact) of the melt:

$$N = \mu(1-\varphi)[1-(1-\psi)^n] \tag{6}$$

The contiguity ψ depends on the melt volume fraction φ and the dihedral angle θ between the solid grains and the melt; and n is an exponent also depending on ψ (Takei, 2002). The simulations of contiguity applied here are based on the micro-structural model of von Bargen and Waff (1986) which formulates the contiguity ψ as the proportion that the contact area of grains occupy among the total contact area in a partial molten aggregate:

$$\psi = \frac{2A_{\mathrm{gg}}}{2A_{\mathrm{gg}} + A_{\mathrm{gm}}} \tag{7}$$

, where A_{gg} and A_{gm} are the grain-grain contact area and grain-melt contact area per unit volume, respectively. The values of A_{gg} and A_{gm} are calculated from the given melt volume fraction and dihedral angle using polynomial functions:

$$\begin{cases} A_{\mathrm{gg}} = \pi - b_{\mathrm{gg}}\mathrm{power}(\varphi, p_{\mathrm{gg}}) \\ A_{\mathrm{gm}} = b_{\mathrm{gm}}\mathrm{power}(\varphi, p_{\mathrm{gm}}) \end{cases} \tag{8}$$

The required constants b_{gg}, b_{gm}, p_{gg} and p_{gm} are approximated from quadratic polynomials of the dihedral angle (in degree), of which the values are outlined in von Bargen and Waff (1986). Wimert and Hier-Majumder (2012) indicated this

approximation of contiguities can produce satisfactory fits with experimental measurements from partially molten aggregates with melt volume fractions below 5%.

Combining equations 3—7 enables the contiguity to be expressed as a function of the melt volume fraction φ and dihedral angle θ, i.e. $\psi = \psi(\varphi, \theta)$. Moreover, shear wave speed anomalies ξ caused by partial melting can be formulated as a function with respect to melt volume fraction and dihedral angle:

$$\xi(\varphi, \theta) = \sqrt{\frac{(1-\varphi)\left[1-\left(1-\psi(\varphi,\theta)\right)^{n}\right]}{1-\varphi(1-\rho_{\mathrm{m}}/\rho_{\mathrm{s}})}} \tag{9}$$

We estimate the densities of solid bulk ρ_{s} and melt ρ_{m} using the third-order Birch-Murnaghan equation of state (EOS), as Ghosh et al. (2007) suggested for carbonated peridotite melt. We implement the mathematic approximations using a Python computational toolkit for microscale geodynamic study, named as Multiphase Material Properties forward model (MuMaP, Hier-Majumder, 2017). The modelled shear wave velocity reductions (in percentage) in response to a variety of melt volume fractions and dihedral angles are illustrated in fig. 4. Each of the curves in the cross-plot represents the shear wave velocity reductions caused by the melt with volume fractions from 0 to 5% at a fixed dihedral angle, showing that the velocity in the partially molten aggregates decreases rapidly as the fraction of melt increases. The upward shifting of the curves indicates that, for the same melt volume fraction, a smaller dihedral angle can result in greater reductions in the shear wave speed. However, different combinations of dihedral angles and melt volume fractions may produce the same extent of shear-velocity reduction.

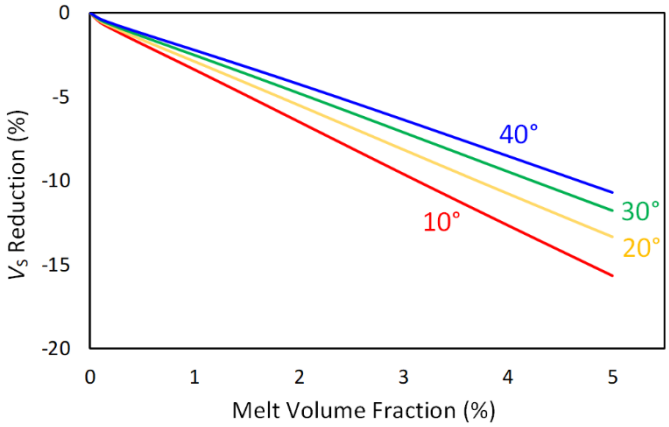

Figure 4 Predicted shear wave velocity reductions for different melt volume fractions and dihedral angles. The corresponding dihedral angles to the curves are annotated on the plot. Each curve shows the velocity reductions caused by changes in melt volume fraction at a fixed dihedral angle

4 Model inversion

The forward modelling approach described in the preceding section predicts the shear wave velocity reductions in response to associated parameters. Alternatively, if seismic data of the LVL are available, it is possible to calculate the velocity reductions as a ratio of the observed velocity over the reference velocities:

$$\xi = \frac{V_S^{\mathrm{obs}}}{V_S^{\mathrm{ref}}(T_0, C)} \tag{10}$$

When embedded with an inversion scheme, the numerical model can be used to deduce the multiple controls on seismic velocities. The inversion procedure can begin with an initial solution that is built upon petrologic and seismological constraints. We then investigate how to exploit and utilize the symmetry of the model, which can allow us to alter the initial solution directly into another solution whilst giving the same

observations. In this way, the additional solutions to the inverse problem can be rapidly derived by repetitively use of the transformation.

4.1 An initial solution based on a priori knowledge

To incorporate the forward model and the observed data in a single framework, we firstly combine eq. 9 and 10:

$$\sqrt{\frac{(1-\varphi)\cdot\left[1-\left(1-\psi(\varphi,\theta)\right)^{n}\right]}{1-\varphi(1-\rho_{\mathrm{m}}/\rho_{\mathrm{s}})}}=\frac{V_{\mathrm{S}}^{\mathrm{obs}}}{V_{\mathrm{S}}^{\mathrm{ref}}(T_0,C)} \tag{11}$$

, which gives four unknowns (i.e. T_0, C, θ and φ) in one equation. To solve melt volume fraction φ from the eq. 11, the reference potential temperature T_0, basalt fraction C and dihedral angle θ need to be specified. We initially assume the reference potential temperature to be 1500 K in the region. We set the basalt fraction at 18%, as suggested in Xu et al. (2008) for common peridotite. The dihedral angle at the grain-melt interface varies with the chemical composition of the melt. For example, Minarik and Watson (1995) proposed dihedral angles varying from 25 to 30° at the interface between carbonate melt and molten aggregates; Mei et al. (2002) suggested a dihedral angle of 28° for molten aggregates with hydrous basalt melt. Here we initially assume a dihedral angle of θ = 25°. Given these *a priori* assumptions, T_0, C and θ are specified, and hence the melt volume fraction can be solved from eq. 11.

We then calculate the corresponding melt volume fraction φ using a modified Newton-Raphson root-search algorithm (Press et al., 2007, chap. 9.1), same as the calculation in Hier-Majumder and Tauzin (2017). The algorithm begins with a bracket

for the melt volume fraction between 1×10^{-4}% and 10% and iterates the searching process until a convergence of 10^{-4}% is achieved in the inferred fraction. Figure 5 shows the initial solution derived from the inversion using the seismic observations and the constraints on T_0, C and θ. The melt fractions in the region vary spatially and yields an average of 0.72%. The synthetic velocities reproduced from the forward model (fig. 5c) proves a good match to the real observations (fig. 1d).

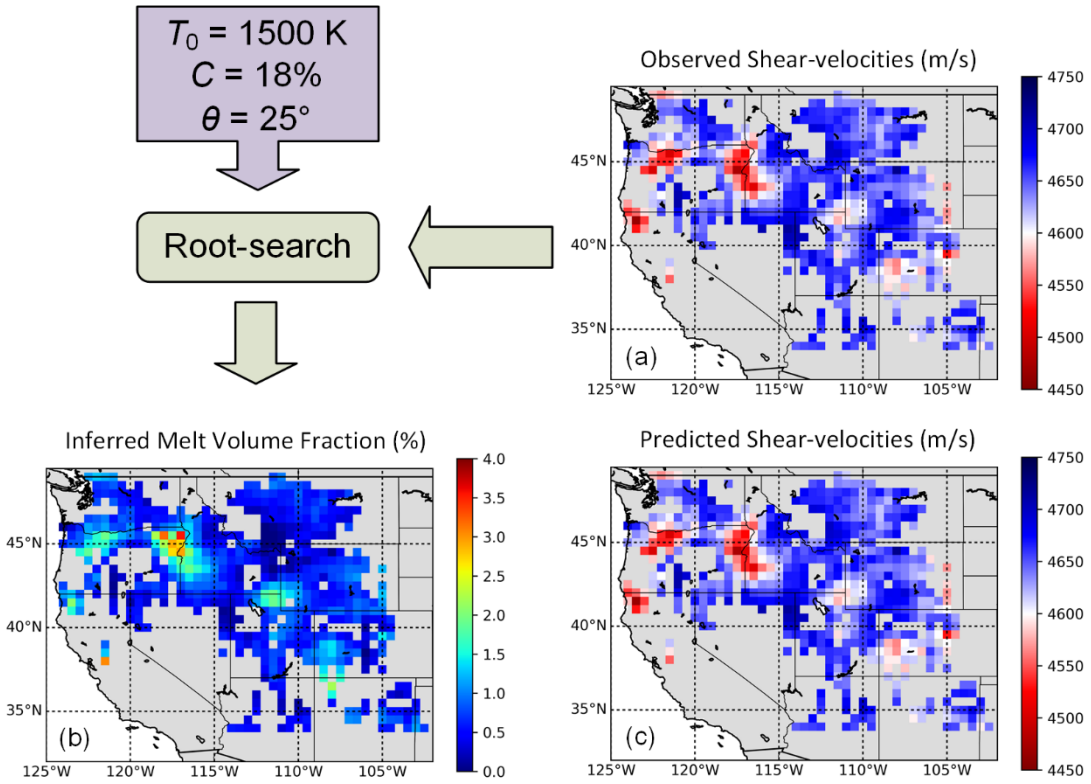

Figure 5 An initial solution found from the inverse problem. The observed shear wave velocities (a) and reference values of T_0, C and θ are used to provide constraints on the inversion. A particular inference of the melt vol. % within the LVL (b) is then generated using a root-search approach. The regionally averaged fraction is calculated as 0.72% given T_0 = 1500 K, C = 18% and θ = 25°. Using the inferred melt vol. % and the reference values, shear wave velocities (c) can be reproduced from the forward model

4.2 Symmetric transformation

The above calculation generates a single solution to the inverse problem. Since the inverse problem is non-unique with respect to the input parameters T_0, C and θ, there are, in principle, an infinite number of alternative solutions that can reproduce identical seismic observations. Here we develop a quantitative approach to prove the non-uniqueness and, more crucially, the transformation from an existing solution to an alternative solution. The symmetry of the numerical model is found by properly modifying the input parameters to obtain an unchanged output model. To start with, we formulate the forward model of shear wave speed as:

$$\boldsymbol{V}_{\mathrm{S}} = F(T_0, C, \theta, \boldsymbol{\varphi}) \tag{12}$$

, where $\boldsymbol{V}_{\mathrm{S}}$ is the shear wave speeds in the LVL beneath the seismic sites; F denotes a general, non-linear function (in this work, F is the forward model from the code MuMaP_fwd) and $\boldsymbol{\varphi}$ is a vector of melt volume fractions in the LVL. Note that 583 seismic sites are analysed in this study, and hence the vector lengths are 583 for both $\boldsymbol{V}_{\mathrm{S}}$ and $\boldsymbol{\varphi}$. We then generate three perturbations δT_0, δC and $\delta\theta$ respectively into the three variables T_0, C and θ. These small changes in the model inputs thus give rise to residuals in the modelled velocities, i.e. $\Delta\boldsymbol{V}_{\mathrm{S}}$. This can be written as:

$$\Delta\boldsymbol{V}_{\mathrm{S}} = F(T_0 + \delta T_0, C + \delta C, \theta + \delta\theta, \boldsymbol{\varphi}) - F(T_0, C, \theta, \boldsymbol{\varphi}) \tag{13}$$

, which may be approximated in a linear form using the first-order Taylor's series:

$$\frac{\partial F}{\partial T_0}\delta T_0 + \frac{\partial F}{\partial C}\delta C + \frac{\partial F}{\partial \theta}\delta\theta = \Delta\boldsymbol{V}_{\mathrm{S}} \tag{14}$$

334 , where $\partial F/\partial T_0$, $\partial F/\partial C$ and $\partial F/\partial \theta$ are finite derivatives of the function F with

335 respect to T_0, C and θ. We then calculate changes required in the melt volume

336 fractions (i.e. $\delta\boldsymbol{\varphi}$) to compensate the changes in velocities resulting from the

337 perturbations. This can be expressed as:

$$F(T_0 + \delta T_0, C + \delta C, \theta + \delta\theta, \boldsymbol{\varphi} + \delta\boldsymbol{\varphi}) - F(T_0, C, \theta, \boldsymbol{\varphi}) = \mathbf{0} \quad (15)$$

338 Approximation based on the Taylor's series gives:

$$\frac{\partial F}{\partial T_0}\delta T_0 + \frac{\partial F}{\partial C}\delta C + \frac{\partial F}{\partial \theta}\delta\theta + \frac{\partial F}{\partial \boldsymbol{\varphi}}\delta\boldsymbol{\varphi} = \mathbf{0} \quad (16)$$

339 , where $\partial F/\partial\boldsymbol{\varphi}$ is the finite derivative of the function F with respect to $\boldsymbol{\varphi}$. We then

340 solve $\delta\boldsymbol{\varphi}$ by combining eq. 14 and 16:

$$\delta\boldsymbol{\varphi} = -\frac{\Delta\boldsymbol{V}_\mathbf{S}}{\partial F/\partial\boldsymbol{\varphi}} \quad (17)$$

341 In this equation, $\partial F/\partial\boldsymbol{\varphi}$ can be calculated from the forward model. We make small

342 changes in $\boldsymbol{\varphi}$ and then run the model to predict the corresponding velocities. The

343 values of $\partial F/\partial\boldsymbol{\varphi}$ are given by the difference in the modelling outputs divided by the

344 small changes in $\boldsymbol{\varphi}$. Note that $\delta\boldsymbol{\varphi}$, $\partial F/\partial\boldsymbol{\varphi}$ and $\Delta\boldsymbol{V}_\mathrm{S}$ are all vectors with a length of 583

345 as there are 583 locations in total. Given the perturbations δT_0, δC and $\delta\theta$ and the

346 required adjustments in melt volume fractions $\delta\boldsymbol{\varphi}$, the model $F(T_0 + \delta T_0, C + \delta C, \theta +$

347 $\delta\theta, \boldsymbol{\varphi} + \delta\boldsymbol{\varphi})$ can produce the same shear wave speeds as given by the initial solution.

348 The new solution can then be used as a basis for another transformation. Iterative

349 transformation can therefore derive all the additional solutions to the inverse problem.

350

4.3 Calculating multiple solutions

Using the forward model and symmetric transformation, we then examine the entire parameter space and calculate alternative solutions. The parameter space can be considered as a 3-D volume of which the three dimensions are potential temperature (T_0), basalt fraction (C) and dihedral angle (θ). We define the ranges of the parameters as 1400 to 1800 K in potential temperature, 10 to 40% in basalt fraction and 10° to 40° in dihedral angle. We also set the increments at 10 K in potential temperature, 1% in basalt fraction and 1° in dihedral angle. Therefore, the parameter space is finely sampled and thus the transformation approach can apply. Each position in the parameter space can be described using the coordinates in the three dimensions. If a solution exists in position (T_0, C, θ), then the corresponding melt volume fraction vector can be written as $\boldsymbol{\varphi}(T_0, C, \theta)$. Once a solution is found, the solutions in neighbouring positions can also be determined. Because the transformation can be applied both forward and backward, six neighbouring solutions should be examined, including $\boldsymbol{\varphi}(T_0 + \delta T_0, C, \theta)$, $\boldsymbol{\varphi}(T_0 - \delta T_0, C, \theta)$, $\boldsymbol{\varphi}(T_0, C + \delta C, \theta)$, $\boldsymbol{\varphi}(T_0, C - \delta C, \theta)$, $\boldsymbol{\varphi}(T_0, C, \theta + \delta\theta)$ and $\boldsymbol{\varphi}(T_0, C, \theta - \delta\theta)$. We calculate the additional solutions through the following procedure:

(1) Create an empty list. Add the coordinate of the initial solution into the list.

(2) For each solution in the list, calculate the solutions in the neighbouring positions that are inside of the parameter space but not existing in the list.

(3) Add the solutions found in step (2) into the list.

(4) Return to step (2) and repeat the workflow until no new solution can be

added into the list.

Note that this is different from a brute-force search which involves a root-searching approach for calculating the melt volume fraction beneath every location given different combinations of T_0, C and θ. In contrast, the symmetric transformation is straightforward as it can simultaneously derive the melt volume fraction beneath the whole area. Since this method works directly on the behaviour of the solution with respect to perturbations, it also allows us to predict regions where solution does not exist and the solution containing the lowest possible average melt fractions, which was intractable with the method described by Hier-Majumder et al. (2014).

4.4 Complete solutions to the inverse problem

Using the above computational procedure, we derive all the solutions in the parameter space. All the possible solutions can reproduce the same synthetic shear wave velocities from the forward model. Significant spatial variations in the inverted melt volume are found in every solution. Because the melt volume fraction should always be non-negative, the calculated vectors of $\boldsymbol{\varphi}$ where one or more negative values exist should be removed. Given this requirement, limits can be placed to bound the symmetric transformation, i.e. not every combination of potential temperatures, basalt fractions and dihedral angles in the parameter space is compatible with the seismic observations, though not a unique solution to the inverse problem can be found. Example of the variations in calculated melt volume fractions and the transformation limits in the multiple controlling factors are demonstrated in fig. 6.

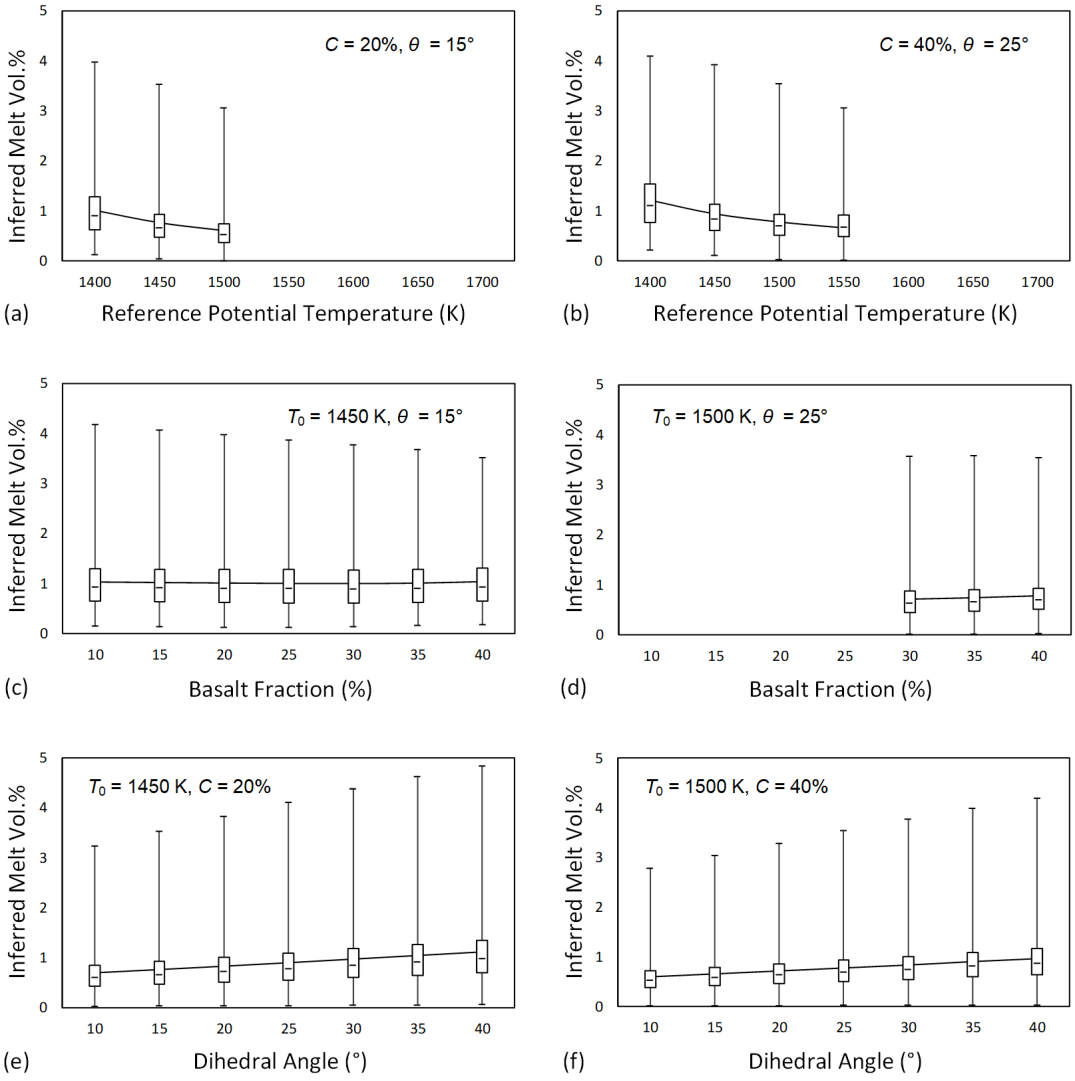

395

396 **Figure 6** Series of box-plots showing the estimated melt vol.% beneath all locations with median

397 indicated by the horizontal line within each box, upper/lower quartiles indicated by the

398 upper/lower edges of the box and maximum/minimum indicated by whiskers of the boxes. (a) & (b)

399 Inferred melt vol.% as a function of reference potential temperature with fixed basalt fraction and

400 dihedral angles. (c) & (d) Inferred melt vol.% as a function of basalt fractions with fixed reference

401 potential temperature and dihedral angle. (e) & (f) Inferred melt vol.% as a function of dihedral

402 angle with fixed reference potential temperature and basalt fractions. Note that no solution can be

403 found given $T_0 \geqslant 1500$ in (a), $T_0 \geqslant 1550$ K in (b) and $C \leqslant 30\%$ in (d)

404

405 The model output illustrated in fig. 7 is an end-member solution showing that the
406 lowest possible averaged melt volume fraction is 0.51%, associated with T_0 = 1550 K, C
407 = 40% and θ = 10°. In this solution, the melting is not predicted beneath some regions,
408 for instance at the triple border between Idaho, Montana and Wyoming. Considering
409 the sharp boundary atop the LVL, this may just be an artefact because the variations in
410 solid bulk are unlikely to produce the rapid velocity reductions. However, this solution
411 is still meaningful since it places a lower-bound below the regional-averaged melt
412 volume fraction within the observed LVL. In contrast, the highest possible averaged
413 melt volume fraction that exists in the parameter space yields 1.47%, associated with
414 T_0 = 1400 K, basalt fraction C = 10% and dihedral angel θ = 10°, as shown in fig. 8.
415 Examples of the trade-offs between the estimated melt volume fraction below a given
416 location and the multiple controls are displayed in fig. 9 by cross-plotting the estimates
417 and the corresponding controlling factors. Whilst the forward model used here is non-
418 linear, application of the proposed method has indicated the trajectories that link
419 together the multiple solutions in the parameter space.
420

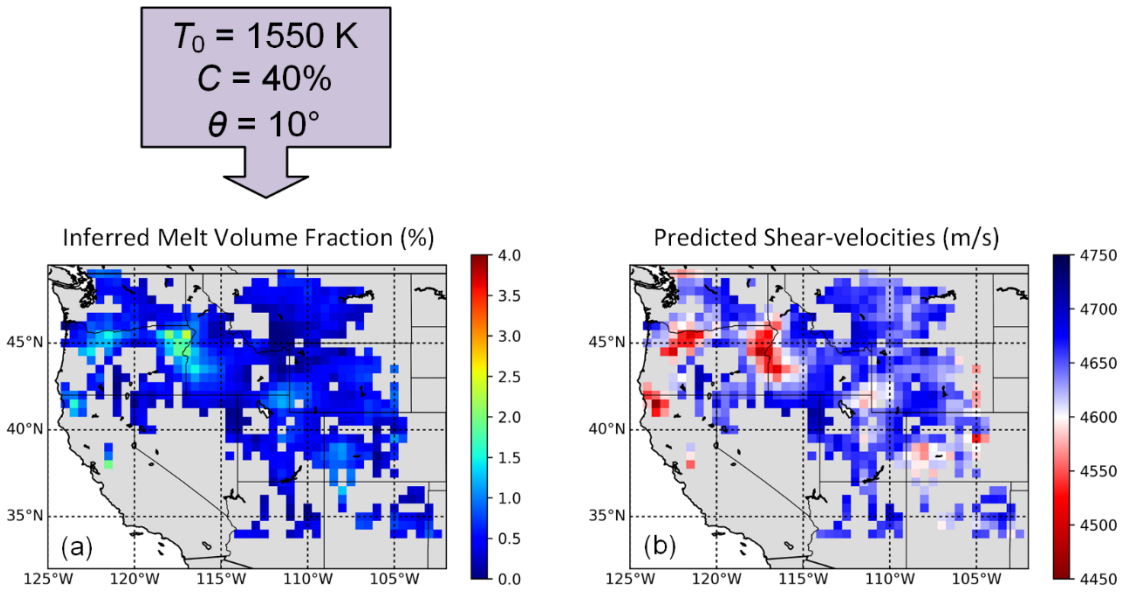

421

422 **Figure 7** The end-member solution with the minimum melt vol. % within the LVL beneath the w.

423 The regional averaged melt vol. % is 0.51% given T_0 = 1550 K, C = 40% and θ = 10°. Note that this

424 solution is directly derived from the initial solution, rather than from a brute-force search

425

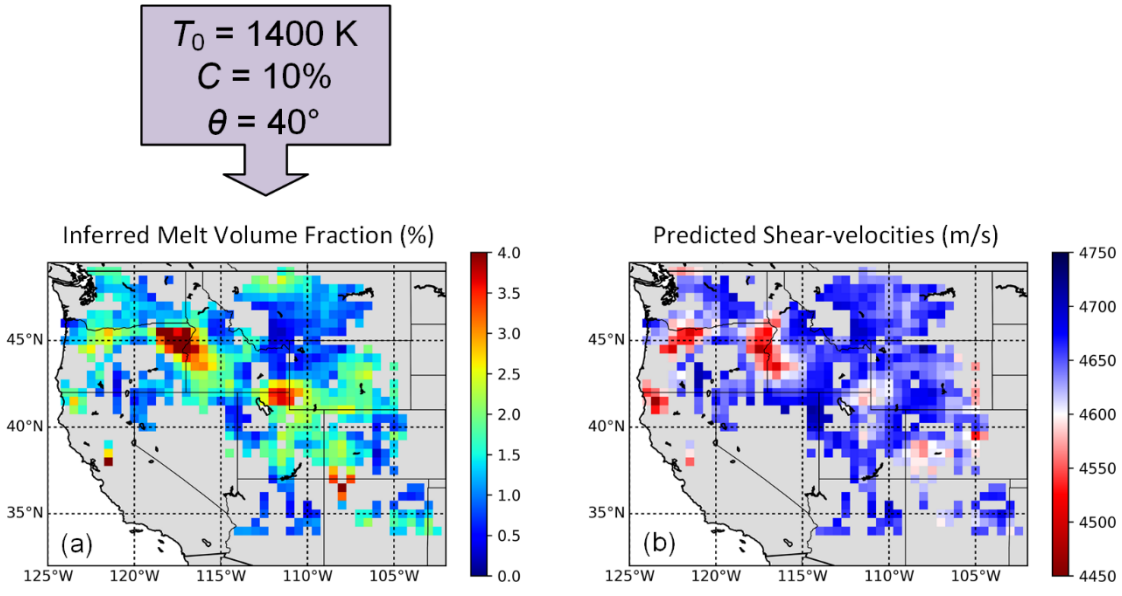

426

427 **Figure 8** The end-member solution with the maximum melt vol. % within the LVL beneath the

428 region. The regional averaged melt vol. % is 1.47% given T_0 = 1400 K, C = 10% and θ = 40°. Note

429 that this solution is directly derived from the initial solution, rather than from a brute-force search

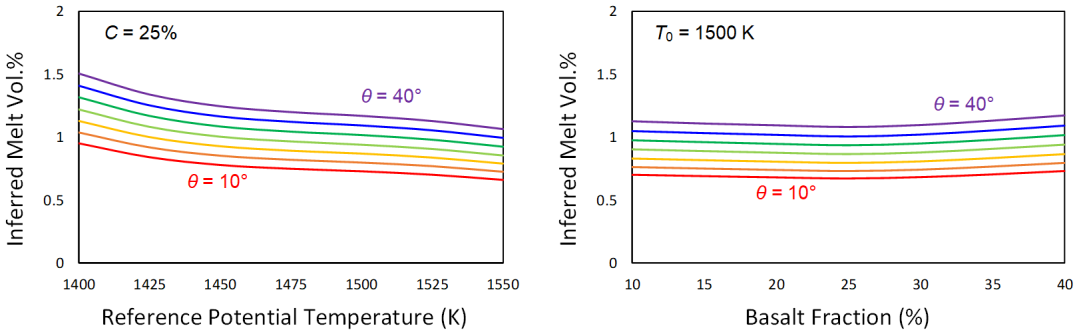

Figure 9 Cross-plots of inferred melt volume fraction beneath 106°W, 35°N (label A in fig. 1a) versus (a) the reference potential temperature for different dihedral angles ranging from 10° to 40° (annotated on the plot) with constant intervals of 5° given a fixed basalt composition and (b) the basalt fraction in the bulk composition for a range of different dihedral angles given a fixed potential temperature

5 Discussion

Using a numerical inversion approach, we have examined the LVL at 350 km underneath the western US. The shear-velocity anomalies and impedance contrasts in this zone have been thought to indicate a small fraction of volatile-rich melt (Hier-Majumder and Tauzin, 2017) released either by the decarbonation during the Farallon slab subduction (Thomson et al., 2016) or by the dehydration from the upwelling of the Yellowstone mantle plume or small-scale convection within the MTZ (Bercovici and Karato, 2003; Richard and Bercovici, 2009; Zhang et al., 2018). Despite the presence of petrological and geochemical evidences of melting near the MTZ, determination of the quantity of melting from seismic signatures remains hard work owing to the trade-offs that exist between various controlling factors. Due to the lack of geophysical and geochemical constraints, it is difficult, if not impossible, to distinguish the individual

449 effects of temperature, composition and partial melting. A recent study has further
450 suggested that these multiple controls are strongly correlated, leading to a
451 disagreement between the experimental measurements and theoretical estimates
452 (Freitas et al., 2019).

453 Our numerical scheme based on a symmetry is able to cover all solutions. Using a
454 forward model, we firstly generate an arbitrary solution assuming T_0 = 1500 K, C = 18%
455 and θ = 25°. This is a successful solution as the shear wave velocities it predicts are
456 consistent with the observations. The inverse problem is then linearized to find
457 neighbouring solutions to the initial solution. As the controlling parameters have only a
458 limited range of plausible values (in this work 1400 ≤ T_0 ≤ 1800 K, 10% ≤ C ≤ 40% and
459 10° ≤ θ ≤ 40°), the symmetry gives a quasi-complete set of solutions subject to the
460 necessary constraint that the melt volume fraction in the upper mantle must always be
461 non-negative. This constraint can be justified as the effects of temperature and
462 composition are already taken into account. Given the above treatment, it is then a
463 simple matter to find the combinations of parameters that reveals the end-member
464 possibilities (e.g. maximum and minimum degrees of partial melting).

465 The modelling results show that a regional-averaged melt volume fraction of
466 approximately 0.51% is necessary to explain the sharp shear-velocity reductions at 350
467 km beneath the western US. This is the minimum extent of melting required to
468 produce the observed LVL, whatever the solid mantle conditions and the geometry of
469 the melt are. As Hier-Majumder and Courtier (2011) suggested, at such a small level of
470 melting, a near neutrally buoyant melt can migrate over the LVL due to surface

tension, whereas the drainage efficiency of both buoyant and dense melts is likely insignificant.

As no solution has been found to be associated with a reference potential temperature higher than 1550 K, we can place an upper-bound on the variations in the reference potential temperature. The modelling output also shows that the range of variations in basalt fraction depends on the assumed reference potential temperature. At a low reference potential temperature (e.g. 1400 K), the basalt fraction may vary from 10% to 40%. In contrast, at a higher reference potential temperature, solutions can only be in the basaltic-rich zone (e.g. fig. 6d). For instance, Hier-Majumder and Tauzin (2017) estimated the reference potential temperature as approximately 1550 K. If this is the case, then we can make a statement that the basalt fraction in the LVL beneath the western US is no less than 40%. Hence, whilst the thermal and compositional conditions are still under-constrained, our model work offers more reliable information about the mantle physical properties.

In addition, our inverse method unravels trade-offs between parameters. As the forward model is non-linear, there is no simple analytical tool for determining these competing effects. The numerical approach proposed here allows estimating the rates of change in the inferred melt volume fraction caused by changes in other parameters. According to the modelling outputs, the significance of the trade-offs between inferred melt volume fractions and other parameters can be summarized as:

(1) For a given dihedral angle and a given basalt fraction, the inferred melt volume fractions present a strong negative correlation with the assumed

reference potential temperatures (fig. 6a & b).

(2) For a given reference potential temperature and a given dihedral angle, the inferred melt volume fractions are insensitive to the assumed basalt fractions (fig. 6c & d).

(3) For a given reference potential temperature and a given basalt fraction, the inferred melt volume fractions present a modest positive correlation with the assumed dihedral angles (fig. 6e & f).

In this analysis, a number of assumptions are made about the mantle: it is in a state of chemical disequilibrium (described as a mechanical mixture of basalt and harzburgite), melt films are not playing a role in velocity reduction, the transition zone thickness reflects temperature variations, the Clapyron slope is known, and receiver function estimates of MTZ thickness are accurate.

This study calculates the temperature variations from the thickness of the MTZ using the empirical correlation proposed by Tauzin and Ricard (2014). The empirical model relies on several assumptions, for example that only temperature varies MTZ thickness and that no vertical variation occurs in temperature from the MTZ to the LVL. As observed from tomographic models (with low vertical resolution), the MTZ has consistent structures over the whole range of depth, in particular the stalled Juan de Fuca/Farallon slab (Burdick et al., 2008; Schmandt et al., 2011; Hier-Majumder and Tauzin, 2017). Although an entirely consistent MTZ should not be expected, dealing with the absolute topography of discontinuities to infer the temperatures would likely introduce more uncertainties, as would require a precise correction of the effect of

515 shallow velocity heterogeneities from 3-D tomographic models, which have their own
516 limitations.

517 Another assumption involved here is that one can extract reliable MTZ thickness
518 from receiver functions, while interference effects from seismic phases that do not
519 interact with MTZ boundaries can be neglected. It has indeed been shown through
520 modeling that the effect of interfering phases is small (Tauzin et al., 2013). The move-
521 out of these phases is different from the one from direct conversions (Guan and Niu,
522 2017) and stacking along move-out curves for direct conversions is efficient in
523 removing their effect. Besides, slant-stack diagrams and slowness weighted stacking
524 (e.g. Guan and Niu, 2017; Hier-Majumder and Tauzin, 2017) show no evidence for
525 interference effects in several locations of the western US.

526 Apart from the primary controls on the seismic velocities we have investigated,
527 there are other factors that can influence the seismic wave speeds. In this work, the
528 Clapeyron slopes γ are set to values from a compilation of experimentally obtained
529 values (Tauzin and Ricard, 2014). The values of matrix density ρ_s and melt density ρ_m
530 are set to constants as suggested in previous studies. The thickness of MTZ applied
531 here are also from supplementary dataset whereas alternative empirical models (e.g.
532 Keifer and Dueker, 2019) would produce different scenarios. These additional
533 complications can lead to substantial uncertainties in estimated melt volume fractions.
534 However, the inversion technique presented here is independent from the forward
535 model and can easily be adapted to include these factors. While in this paper the
536 application of the inversion has been demonstrated using 1-D column simulation, the

technique could be applied to more sophisticated models that are spatially 2-D or 3-D. For future work, we intend to apply our modelling approach to investigating the LVL identified in other regions that differ in tectonic settings, for example, the Hawaii Islands (Huckfeldt et al., 2013) which are dominated by mantle plumes. An effort will be done for accounting for uncertainties from seismic data and propagate it into mantle melting estimates.

6 Conclusions

The interpretation of the observed seismic structures in the upper mantle, like many other geophysical inverse problems, is hampered by the fundamental challenge of non-uniqueness. In this work, we investigate the influence of thermal, compositional and melting effects on the pervasive LVL at 350 km beneath the western US. We develop an inversion scheme, based on the principle of symmetry, for generating the full range of solutions in the parameter space. Although a unique solution is not available, the calculation of an ensemble of solutions allows extracting the properties that are common to all solutions. A key result of our inversion is that a minimum fraction of ~0.5% melt by volume is necessary to explain the seismically anomalous layer in the region. The scheme also encapsulates the ranges of variations in the thermal and compositional factors. Consequently, the application of the proposed inversion technique can provide more robust interpretation of seismic velocity reductions within the mantle.

Acknowledgement

The authors would like to thank Editor Mark Jellinek and two anonymous reviewers for their constructive comments. Jie Xiao acknowledges support from the Strategic Priority Research Program of the Chinese Academy of Sciences (XDA14010103) and China National Major S&T Program (2017ZX05008-002-030). Jie Xiao also wishes to thank China Scholarship Council (CSC) for funding his PhD research. This research is also supported by the European Union's Horizon 2020 research and innovation programme under Benoit Tauzin's Marie Sklodowska-Curie grant agreement 793824.

References

Bercovici, D., and Karato, S.-i., 2003, Whole-mantle convection and the transition-zone water filter: Nature, v. 425, no. 6953, p. 39.

Burdick, S., Li, C., Martynov, V., Cox, T., Eakins, J., Mulder, T., Astiz, L., Vernon, F. L., Pavlis, G. L., and van der Hilst, R. D., 2008, Upper mantle heterogeneity beneath North America from travel time tomography with global and USArray transportable array data: Seismological Research Letters, v. 79, no. 3, p. 384-392.

Courtier, A. M., and Revenaugh, J., 2007, Deep upper-mantle melting beneath the Tasman and Coral Seas detected with multiple ScS reverberations: Earth and Planetary Science Letters, v. 259, no. 1-2, p. 66-76.

Fee, D., and Dueker, K., 2004, Mantle transition zone topography and structure beneath the Yellowstone hotspot: Geophysical Research Letters, v. 31, no. 18.

581 Freitas, D., Manthilake, G., Chantel, J., Bouhifd, M., and Andrault, D., 2019,
582 Simultaneous measurements of electrical conductivity and seismic wave
583 velocity of partially molten geological materials: effect of evolving melt texture:
584 Physics and Chemistry of Minerals, p. 1-17.
585 Gao, W., Matzel, E., and Grand, S. P., 2006, Upper mantle seismic structure beneath
586 eastern Mexico determined from P and S waveform inversion and its
587 implications: Journal of Geophysical Research: Solid Earth, v. 111, no. B8.
588 Ghosh, S., Ohtani, E., Litasov, K., Suzuki, A., and Sakamaki, T., 2007, Stability of
589 carbonated magmas at the base of the Earth's upper mantle: Geophysical
590 research letters, v. 34, no. 22.
591 Guan, Z., and Niu, F., 2017, An investigation on slowness-weighted CCP stacking and its
592 application to receiver function imaging: Geophysical Research Letters, v. 44,
593 no. 12, p. 6030-6038.
594 Hier-Majumder, S., 2017, MuMaP_fwd, Version: 1.0, Zenodo,
595 http://doi.org/10.5281/zenodo.1040971.
596 Hier-Majumder, S., and Abbott, M. E., 2010, Influence of dihedral angle on the seismic
597 velocities in partially molten rocks: Earth and Planetary Science Letters, v. 299,
598 no. 1-2, p. 23-32.
599 Hier-Majumder, S., and Courtier, A., 2011, Seismic signature of small melt fraction atop
600 the transition zone: Earth and Planetary Science Letters, v. 308, no. 3-4, p. 334-
601 342.

602 Hier-Majumder, S., Keel, E. B., and Courtier, A. M., 2014, The influence of temperature,
603 bulk composition, and melting on the seismic signature of the low-velocity layer
604 above the transition zone: Journal of Geophysical Research: Solid Earth, v. 119,
605 no. 2, p. 971-983.
606 Hier-Majumder, S., and Tauzin, B., 2017, Pervasive upper mantle melting beneath the
607 western US: Earth and Planetary Science Letters, v. 463, p. 25-35.
608 Huckfeldt, M., Courtier, A. M., and Leahy, G. M., 2013, Implications for the origin of
609 Hawaiian volcanism from a converted wave analysis of the mantle transition
610 zone: Earth and Planetary Science Letters, v. 373, p. 194-204.
611 Jasbinsek, J., and Dueker, K., 2007, Ubiquitous low-velocity layer atop the 410-km
612 discontinuity in the northern Rocky Mountains: Geochemistry, Geophysics,
613 Geosystems, v. 8, no. 10.
614 Jasbinsek, J. J., Dueker, K. G., and Hansen, S. M., 2010, Characterizing the 410 km
615 discontinuity low-velocity layer beneath the LA RISTRA array in the North
616 American Southwest: Geochemistry, Geophysics, Geosystems, v. 11, no. 3.
617 Katsura, T., Yoneda, A., Yamazaki, D., Yoshino, T., and Ito, E., 2010, Adiabatic
618 temperature profile in the mantle: Physics of the Earth and Planetary Interiors,
619 v. 183, no. 1-2, p. 212-218.
620 Keifer, I., and Dueker, K., 2019, Testing the hypothesis that temperature modulates
621 410 and 660 discontinuity topography beneath the eastern United States: Earth
622 and Planetary Science Letters, v. 524, p. 115723.

623 Kennett, B., and Engdahl, E., 1991, Traveltimes for global earthquake location and
624 phase identification: Geophysical Journal International, v. 105, no. 2, p. 429-
625 465.
626 Mavko, G. M., 1980, Velocity and attenuation in partially molten rocks: Journal of
627 Geophysical Research: Solid Earth, v. 85, no. B10, p. 5173-5189.
628 Mei, S., Bai, W., Hiraga, T., and Kohlstedt, D., 2002, Influence of melt on the creep
629 behavior of olivine–basalt aggregates under hydrous conditions: Earth and
630 Planetary Science Letters, v. 201, no. 3-4, p. 491-507.
631 Minarik, W. G., and Watson, E. B., 1995, Interconnectivity of carbonate melt at low
632 melt fraction: Earth and Planetary Science Letters, v. 133, no. 3-4, p. 423-437.
633 Morra, G., Yuen, D. A., Boschi, L., Chatelain, P., Koumoutsakos, P., and Tackley, P.,
634 2010, The fate of the slabs interacting with a density/viscosity hill in the mid-
635 mantle: Physics of the Earth and Planetary Interiors, v. 180, no. 3-4, p. 271-282.
636 Press, W. H., Teukolsky, S. A., Vetterling, W. T., and Flannery, B. P., 2007, Numerical
637 recipes 3rd edition: The art of scientific computing, Cambridge university press,
638 p. 445.
639 Revenaugh, J., and Sipkin, S., 1994, Seismic evidence for silicate melt atop the 410-km
640 mantle discontinuity: Nature, v. 369, no. 6480, p. 474.
641 Richard, G. C., and Bercovici, D., 2009, Water-induced convection in the Earth's mantle
642 transition zone: Journal of Geophysical Research: Solid Earth, v. 114, no. B1.

643 Schaeffer, A., and Bostock, M., 2010, A low-velocity zone atop the transition zone in
644 northwestern Canada: Journal of Geophysical Research: Solid Earth, v. 115, no.
645 B6.
646 Schmandt, B., Dueker, K., Hansen, S., Jasbinsek, J. J., and Zhang, Z., 2011, A sporadic
647 low-velocity layer atop the western US mantle transition zone and short-
648 wavelength variations in transition zone discontinuities: Geochemistry,
649 Geophysics, Geosystems, v. 12, no. 8.
650 Song, T.-R. A., Helmberger, D. V., and Grand, S. P., 2004, Low-velocity zone atop the
651 410-km seismic discontinuity in the northwestern United States: Nature, v. 427,
652 no. 6974, p. 530.
653 Takei, Y., 1998, Constitutive mechanical relations of solid-liquid composites in terms of
654 grain-boundary contiguity: Journal of Geophysical Research: Solid Earth, v. 103,
655 no. B8, p. 18183-18203.
656 Takei, Y., 2002, Effect of pore geometry on Vp/Vs: From equilibrium geometry to crack:
657 Journal of Geophysical Research: Solid Earth, v. 107, p. 2043.
658 Tauzin, B., and Ricard, Y., 2014, Seismically deduced thermodynamics phase diagrams
659 for the mantle transition zone: Earth and Planetary Science Letters, v. 401, p.
660 337-346.
661 Tauzin, B., Van Der Hilst, R. D., Wittlinger, G., and Ricard, Y., 2013, Multiple transition
662 zone seismic discontinuities and low velocity layers below western United
663 States: Journal of Geophysical Research: Solid Earth, v. 118, no. 5, p. 2307-
664 2322.

665 Thomson, A. R., Walter, M. J., Kohn, S. C., and Brooker, R. A., 2016, Slab melting as a
666 barrier to deep carbon subduction: Nature, v. 529, no. 7584, p. 76.
667 Vinnik, L., and Farra, V., 2007, Low S velocity atop the 410-km discontinuity and mantle
668 plumes: Earth and Planetary Science Letters, v. 262, no. 3-4, p. 398-412.
669 Vinnik, L., Ren, Y., Stutzmann, E., Farra, V., and Kiselev, S., 2010, Observations of S410p
670 and S350p phases at seismograph stations in California: Journal of Geophysical
671 Research: Solid Earth, v. 115, no. B5.
672 von Bargen, N., and Waff, H. S., 1986, Permeabilities, interfacial areas and curvatures
673 of partially molten systems: results of numerical computations of equilibrium
674 microstructures: Journal of Geophysical Research: Solid Earth, v. 91, no. B9, p.
675 9261-9276.
676 Wimert, J., and Hier-Majumder, S., 2012, A three-dimensional microgeodynamic model
677 of melt geometry in the Earth's deep interior: Journal of Geophysical Research:
678 Solid Earth, v. 117, no. B4.
679 Xiao, J., and Waltham, D., 2019, Non-uniqueness and symmetry in stratigraphic
680 interpretations: A quantitative approach for determining stratal controls:
681 Sedimentology, v. 66, no. 5, p. 1700-1715.
682 Xu, W., Lithgow-Bertelloni, C., Stixrude, L., and Ritsema, J., 2008, The effect of bulk
683 composition and temperature on mantle seismic structure: Earth and Planetary
684 Science Letters, v. 275, no. 1-2, p. 70-79.

685 Yoshino, T., Takei, Y., Wark, D. A., and Watson, E. B., 2005, Grain boundary wetness of
686 texturally equilibrated rocks, with implications for seismic properties of the
687 upper mantle: Journal of Geophysical Research: Solid Earth, v. 110, no. B8.
688 Zhang, Z., Dueker, K. G., and Huang, H.-H., 2018, Ps mantle transition zone imaging
689 beneath the Colorado Rocky Mountains: Evidence for an upwelling hydrous
690 mantle: Earth and Planetary Science Letters, v. 492, p. 197-205.
691